Magnetic Resonance in Medicine 61:381–390 (2009)

A Multispectral Three-Dimensional Acquisition Technique for Imaging Near Metal Implants

Kevin M. Koch,* John E. Lorbiecki, R. Scott Hinks, and Kevin F. King

Metallic implants used in bone and joint arthroplasty induce severe spatial perturbations to the B_0 magnetic field used for high-field clinical magnetic resonance. These perturbations distort slice-selection and frequency encoding processes applied in conventional two-dimensional MRI techniques and hinder the diagnosis of complications from arthroplasty. Here, a method is presented whereby multiple three-dimensional fast-spin-echo images are collected using discrete offsets in RF transmission and reception frequency. It is demonstrated that this multi acquisition variable-resonance image combination technique can be used to generate a composite image that is devoid of slice-plane distortion and possesses greatly reduced distortions in the readout direction, even in the immediate vicinity of metallic implants. Magn Reson Med 61:381–390, 2009.

Key words: MRI of arthroplasty; metal implants; image artifacts; 3D imaging

INTRODUCTION

Total joint replacement (*arthroplasty*) treatments for degenerative joint conditions are increasing at a steady rate. Between 1990 and 2002, the number primary arthroplasty procedures in the United States increased by 62% for total hip replacements and by 195% for total knee replacements. Over the same time period, the numbers of *revision procedures* (surgical replacement of problematic joint prostheses) increased by 79% for hips and 192% for knees (1). The need for arthroplasty revision is accelerating significantly due to the increased frequency of primary arthroplasty procedures and the younger ages at which these procedures are being performed. Statistical projections estimate that by 2030, arthroplasty revisions in the United States will increase from 2005 levels by 137% for hips and 601% for knees (2).

Complications from arthroplasty procedures are often traced to implant wear resulting from routine joint operation (3). Such wear generates particulate matter from microabrasion and microadhesion processes on implant surfaces (4) and can induce a macrophage-mediated immune response in the periprosthetic vicinity. Although these implant particulates can be successfully identified and attacked by macrophages, they cannot be properly digested. This results in sustained increases of osteoclast activity and ultimately to resorption of periprosthetic bone (5). This resorption can further become chronic, leading to osteolysis and eventual aseptic loosening of implants.

Diagnosis of osteolysis and aseptic loosening is a challenging task. Many patients remain asymptomatic of either condition, even when suffering from significant bone loss (6). Furthermore, conventional radiographs often fail in diagnosing pathological conditions that are later identified through more invasive assessments (7). Computerized tomography (CT) can more successfully identify patterns of bone loss and osteolytic lesions (8), but also subjects patients to significant doses of ionizing radiation and lacks the soft-tissue contrast needed to identify early stages of osteolysis. CT also suffers beam hardening artifacts in the immediate vicinity of metal implants, thus further limiting its diagnostic capabilities of early osteolytic trends.

MR imaging has been shown capable of identifying soft-tissue arthroplasty complications (7,9). The early detection capabilities of MR in diagnosing arthroplasty complications has the potential to both improve the accuracy of revision preparations and reduce the severity of treatment procedures (7). Patient well-being and healthcare costs from arthroplasty procedures could both be improved with enhanced MR diagnostic capabilities.

The present work does not address MR safety considerations of metallic implants, which is a topic that has been studied at length in the literature (10). Instead, the capabilities of MR imaging near implants that have established MR safety/compatibility records are addressed.

Implant-induced perturbations to the static B_0 magnetic field are currently the dominant MR limitation posed by metallic implants. These perturbations significantly disrupt spatial encoding mechanisms used in conventional MR imaging and inhibit early osteolytic detection capabilities. Ceramic implant materials possessing reduced magnetic properties have been developed but have yet to gain wide acceptance among orthopedic surgeons (11). Furthermore, the existing installed base, which is the target of revision-based MR diagnostics, is largely composed of metal implants. Metal-induced B_1 transmission and reception perturbations are an additional consideration in imaging of arthroplasty (12,13). However, near commonly utilized implant materials, these B_1 artifacts are secondary to the overwhelming B_0-related artifacts.

Unconventional methods such as single-point imaging (14), prepolarized MRI (15), and view-angle tilting (VAT) (16) have been proposed and demonstrated to reduce the impact of the implant-induced B_0 distortions (17). However, each of these previously studied approaches possesses significant limitations. Single-point imaging suffers from clinically nonviable acquisition times and low spatial resolution. Prepolarized MRI requires dedicated nonstandard MR system hardware that has only been demonstrated for imaging anatomic extremeties. VAT is inherently a two-dimensional process, and while it can mitigate in-plane distortions, it suffers from blurred point-spread functions and residual distortion in the slice-select dimension. A

Applied Science Laboratory, GE Healthcare, Waukesha, Wisconsin

*Correspondence to: Kevin M. Koch, GE Healthcare, Applied Science Laboratory, 3200 N. Grandview Blvd, W875, Waukesha, WI 53188. E-mail: Kevin.Koch@ge.com

Received 2 July 2008; revised 26 August 2008; accepted 18 September 2008.
DOI 10.1002/mrm.21856
Published online in Wiley InterScience (www.interscience.wiley.com).

promising variation of the VAT technique has recently been demonstrated to reduce the slice-selection distortions inherent to VAT images (18).

Here, an MR imaging strategy based on mutlispectral three-dimensional spatial encoding techniques is shown to enable improved arthroplasty diagnostics. The theoretical and methodological principles of this technique are presented in detail. Phantom and in vivo images around commonly utilized metal implants acquired with the presented technique are shown to have drastically reduced image artifacts when compared with standard high imaging-bandwidth, two-dimensional, fast-spin-echo images currently used for clinical arthroplasty MR imaging. The presented technique is shown to greatly improve MR image quality near metallic implants while maintaining clinically viable scan-times and using standard clinical MR hardware.

THEORY

Image Distortions Near Metal Implants

In the absence of thermal relaxation and chemical shifts, the generalized on-resonance spatially encoded imaging signal for an infinitesimally thin two-dimensional slice is given by

$$s(k_x, k_y) \propto \int_{xy} \rho(x,y) e^{2\pi i \left[k_x\left(x + \frac{2\pi\Delta\nu_0(x,y)}{\gamma G_r}\right) + k_y y\right]} dxdy, \quad [1]$$

where k_x and k_y are, respectively, the readout and conventional (stepped gradient amplitudes) phase-encoded dimensions, G_r is the amplitude of the applied readout gradient, and $\Delta\nu_0(x,y)$ is the frequency offset (in Hz) proportional to the static magnetic field inhomogeneity via the Larmor equation. $\Delta\nu_0$(x,y) measures frequency offsets of spin isochromats precessing at frequencies ν_{off}(x,y) relative to a central reception frequency, ν_0,

$$\Delta\nu_0(x,y) = \nu_{off}(x,y) - \nu_0 = \frac{\gamma}{2\pi}\Delta B_0, \quad [2]$$

where ΔB_0 is the magnetic field inhomogeneity and γ is the gyromagnetic ratio for the imaged nuclei.

Readout gradient amplitudes are ultimately constrained by hardware limitations, but are also determined by the desired readout field of view (FOV_r) and the chosen reception bandwidth (BW_r, given in Hz),

$$G_r = 2\pi \frac{BW_r}{\gamma FOV_r}. \quad [3]$$

SNR considerations often prohibit the use of maximum available BW_r (and corresponding G_r) values for a given FOV_r.

It can readily be observed that the k_y encoding relationship in Eq. [1] is unaffected by $\Delta\nu_0$. Therefore, conventional spatial phase-encoding (using stepped phase-encode gradients as opposed to blipped phase advances such as those utilized in echo-planar imaging) is immune to B_0 inhomogeneity.

Utilizing the Fourier shift-theorem, it is also clear from Eq. [1] that the readout encoding dimension is distorted according to

$$\rho(x,y) \overset{\Delta\nu_0(x,y)}{\longrightarrow} \rho\left(x - \frac{2\pi\Delta\nu_0(x,y)}{\gamma G_r}, y\right). \quad [4]$$

For a 256 sample readout collected at a relatively high sampling bandwidth of ±125 kHz, each 1 kHz of $\Delta\nu_0$ offset corresponds to roughly 1 pixel of spatial displacement.

The spectral dispersion of spins near metal implants is well-outside of the levels typically encountered in magnetic-resonance studies. After static shimming procedures are applied (passive and active), a typical clinical MR system will have B_0 homogeneity over a 45 cm diameter spherical volume (DSV) of at least 1.5 ppm. Active B_0 shimming procedures are used to improve or maintain this level of homogeneity after patients distort the applied B_0 field (19). In the vicinity of metal implants, spectral dispersion upwards of 150 ppm is commonly encountered. In a 1.5T system this corresponds to frequency offsets beyond 10 kHz, which can then result in geometric readout displacements on the order of 10 pixels.

If three-dimensional imaging techniques are utilized, both phase-encoded dimensions are free of distortion. However, when utilizing two-dimensional imaging methods, the effects of B_0 heterogeneity on slice selection processes are significant. Slice selection seeks to excite and refocus the slab

$$z_0 - \delta z/2 < z < z_0 + \delta z/2. \quad [5]$$

This is done by applying a gradient G_s along the slicing dimension while transmitting radiofrequency (RF) radiation at a frequency $\nu_{rf} = \nu_0 + \frac{\gamma}{2\pi} G_s z_0$ and bandwidth $\delta\nu_{rf} = \frac{\gamma}{2\pi} G_s \delta_z$, then receiving at a central frequency ν_0 in the absence of the slice-selection gradient. In the presence of B_0 inhomogeneity, spins within the range

$$z_0 - \delta z/2 < z + \frac{2\pi\Delta\nu_0(x,y,z)}{\gamma G_s} < z_0 + \delta z/2, \quad [6]$$

will be excited. B_0 inhomogeneity will distort the desired slab selection from its intended geometry. Displacement is ultimately determined by the chosen slab (or slice) width δz and the slice-selection gradient G_s. Though slice distortion is a continuous function of $\Delta\nu_0(x,y,z)$, the degree of distortion is largely dictated by the relative magnitudes of $\Delta\nu_0$ and $\delta\nu_{rf}$. If $\Delta\nu_0 \ll \delta\nu_{rf}$, then spins will primarily remain encoded in the desired slice. However, if $\Delta\nu_0 \geq \nu_{rf}$, spins will begin to be excited well outside of the intended selection profiles. Rather than a rectangular slab geometry, more complicated three-dimensional volumes will be excited. Consider a slice-selective spin-echo image where the selective RF pulses are applied with $\delta\nu_{rf} = 2$ kHz. For a spin near an implant at $\Delta\nu_0 = 8$ kHz, this would correspond to a slice-selective misregistration of four slices. Local variations of the through-slice $\Delta\nu_0$ gradient can generate further image artifacts. The effective local through-slice field gradient determines the width of excited or refocused slices. Slice to slice variation of this gradient can result in nonuniform thicknesses that translate into unwanted signal variation.

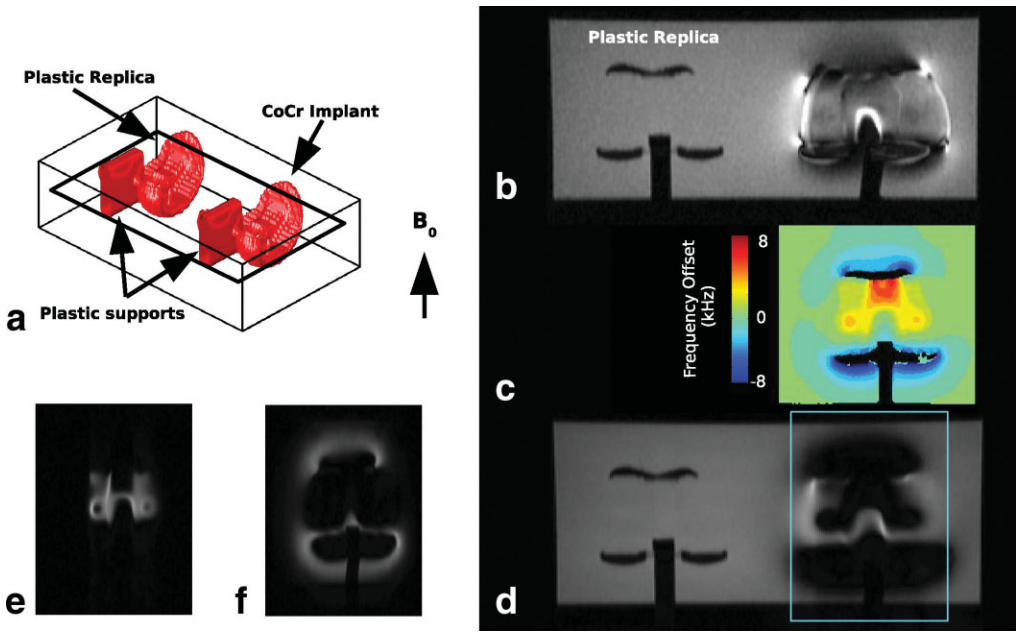

FIG. 1. (**a**) Set up for dual plastic replica and cobalt-chromium femoral implant component phantom. (**b**) Axial 2D-FSE image as indicated in phantom illustration (BW = ±125 kHz, 3 mm slice thickness, selective RF bandwidth of 1 kHz). (**c**) $\Delta\nu_0$ field distribution induced by the cobalt-chromium ($\chi \approx 900$ ppm) component at $B_0 = 1.5$ T. (**d**) Single on-resonance ($\Delta\nu_0^{RT} = 0$) 3D FSE image BW = ±125 kHz, 3 mm slice thickness, Gaussian spectral refocusing RF with FWHM of 2.25 kHz, no slab-selection gradients). (**e**) Extraction indicated by the box in (d) of a similar 3D-FSE image acquired $\Delta\nu_0^{RT} = +2$ kHz off-resonance. (**f**) Extraction of a another such 3D-FSE image acquired $\Delta\nu_0^{RT} = -2$ kHz off-resonance.

Three-Dimensional Imaging Near Metal Implants

Currently, the most common approaches to clinical scanning of arthroplasty patients hinge on two-dimensional fast-spin-echo (2D-FSE) imaging methods (7,9,17,20). The methods presented here apply an alternative strategy utilizing three-dimensional fast-spin echo (3D-FSE) imaging techniques. Although such three-dimensional encoding techniques remove slice-selective distortion near metal implants, they are also more limited in the spectral ranges that can be imaged. Without the application of slice or slab selection gradients, the effective bandwidth of imaged spins is dictated solely by the spectral properties of applied RF pulses. Selective Shinnar-Le Roux (SLR) refocusing pulses are typically limited to only a few kHz in available bandwidth (excitation pulses can inherently achieve higher bandwidths). In the vicinity of metallic implants at field strengths of 1.5T or above, where frequency offsets of 10 kHz are readily found, an on resonance three-dimensional image will therefore not be able to impact a large portion of the spin ensemble.

Figure 1 demonstrates the limitations of conventional two dimensional and three dimensional imaging near metal implants at $B_0 = 1.5$ T. Figure 1a provides the phantom setup for the displayed images. Cobalt-chromium (CoCr) has a magnetic susceptibility of roughly 900 ppm (21), which is nearly 5 times the published magnetic susceptibility of titanium (22). An axial 2D-FSE image acquired with 160^o $\delta\nu_{rf} = 1$ kHz selective SLR refocusing pulses (3 mm slices, $BW_r = \pm 125$ kHz) is presented in Fig. 1b. Figure 1d presents a 3D-FSE image acquired with 3 mm slices, $BW_r = \pm 125$ kHz, 135^o Gaussian (FWHM = 2.25 kHz) refocusing pulses, and no applied slab-selection gradients. In this image, there is a clear signal void around the implant from off-resonance spins not being impacted by the on-resonance RF pulses.

The on-resonance image in Fig. 1d is localized in three dimensions by the central RF transmission and reception frequency ($\nu_0^{RT} = \nu_{rf} = \nu_0$), the spectral properties of the RF transmission pulse, and the $\Delta\nu_0(x,y,z)$ distribution induced by the implant. If the central transmission and reception frequencies are altered according to $\nu_0^{RT} = \nu_0 + \Delta\nu_0^{RT}$, another region of the image space will be localized and collected. Figure 1e,f display 3D-FSE images collected at respective transmission and reception frequency shifts of $\Delta\nu_0^{RT} = +2$ kHz and $\Delta\nu_0^{RT} = -2$ kHz. It is clear that each of the images in Fig. 1d–f occupy a different region of space around the implant. The distinct image formation at each resonance frequency offset is similar in nature to conventional slice-selection. However, the selection process in this case is not accomplished by an externally applied gradient, but is determined by the native $\Delta\nu_0(x,y,z)$ distribution around the implant. This frequency-offset distribution is depicted in Fig. 1c. The spatial coverage of images (Fig. 1d–f) clearly correlates with the displayed frequency distribution. Methods for constructing field maps such as that shown in Fig. 1c are discussed later in this work.

The methods illustrated in Figure 1d–f can be extended to collect a larger series of images collectively spanning the desired sample volume. This is the fundamental principle behind the presented multi-acquisition variable-resonance image combination (MAVRIC) technique. With judicious choices of RF spectral bands and increments of subimage frequency offsets, a complete composite image can be

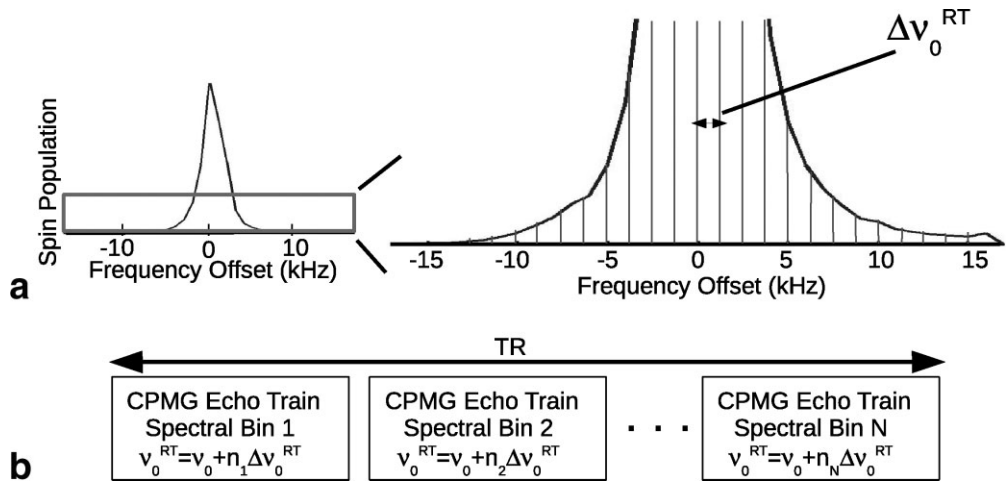

FIG. 2. (**a**) Proton spectrum near a CoCr femoral knee component indicating spectral bin arrangements used in the MAVRIC technique. As indicated, bin separations of $\Delta\nu_0^{RT} = 1$ kHz are utilized. (**b**) Organization of the MAVRIC pulse sequence whereby multiple CPMG echo trains over unique spectral ranges are acquired within a single TR period.

attained via either maximum intensity projection or a sum of squares computation in the image domain.

The MAVRIC method successfully images in extreme off-resonance conditions by breaking abnormally broad spectral distributions into discrete and independently-imaged frequency bins. This enables coverage of very large spectral ranges while simultaneously minimizing off-resonance effects in spatial encoding processes. Each MAVRIC subimage (or spectral bin) only impacts spins resonating within one-half the bandwidth of the applied RF pulses. Thus, the maximum effective $\Delta\nu_0$ offset for the entire MAVRIC image acquisition is far less than the total spectral range across the sample volume. For example, consider a MAVRIC acquisition using 2 kHz RF pulses. If 256 sampled readout is collected at a bandwidth of ± 125 kHz, the maximum absolute displacement in a composite MAVRIC image is roughly 1 pixel, independent of absolute $\Delta\nu_0$ offsets.

METHODS

Magnetic resonance imaging was performed on a 1.5T GE HDx system (GE Healthcare, Waukesha, WI) equipped with 33 mT/m gradients (120 T/m/sec slew rate).

Imaging was performed for three distinct implant scenarios. Phantom A was a CoCr/Ti total hip replacement prosthesis embedded in a cylindrical aqueous phantom (radius 9 cm, length 30 cm) and fitted within an acrylic grid perpendicular to the cylinder's long axis (1 cm grid spacing). Phantom B (depicted in Fig. 1a) was constructed from the CoCr femoral component of a total knee replacement. Along with a plastic molded replica, this implant was mounted in a 28 cm $\times$ 18 cm $\times$ 15 cm aqueous phantom. Finally, in vivo imaging was performed on a 52-year-old male with a 6-year-old CoCr/Ti total knee replacement. The human volunteer was not symptomatic of any complications from the primary arthroplasty procedure and was imaged in accordance with established Investigational Review Board protocols.

RF for Phantom A and the in vivo images was transmitted and received with a single channel GE Quad Knee coil. Phantom B was imaged using a GE body transmit/receive birdcage coil.

Image reconstruction was performed offline in Matlab (Mathworks, Natick, MA) on a Linux workstation.

Pulse Sequence Design

The MAVRIC technique relies upon conventional 3D-FSE acquisition protocols. However, some modification of established methods is required to reduce total scan times and improve the formation of composite MAVRIC images.

Image Interleaving

Individual MAVRIC images operate primarily on independent spin ensembles. Therefore, much like a Cartesian slice-selective imaging technique, the MAVRIC technique can interleave multiple spectrally unique subimages within a single TR period. Such an image interleaving strategy allows freedom of echo time (TE) and repetition time (TR) ratios while maximally utilizing available TR period sampling time.

Figure 2 illustrates the principles of the MAVRIC pulse-sequence structure. A typically encountered spectral distribution near a CoCr femoral knee component is displayed in Fig. 2a. The indicated excised section of this spectrum allows clear observation of its off-resonance components. Lines are indicated in the spectrum where MAVRIC subimages have central ν_0^{RT} frequency offsets. Each spectral setting is separated by $\Delta\nu_0^{RT} = 1$ kHz. The structure of the MAVRIC pulse sequence is illustrated in Fig. 1b. Within a single TR period, multiple Carr-Purcell-Meiboom-Gill (CPMG) echo-trains over unique spectral ranges are acquired. Values of ν_0^{RT} are updated for each echo-train as integer multiples (n_i) of $\Delta\nu_0^{RT}$, where $i = [1, N]$, and N is the number of echo-trains that can be acquired within a single TR period. Acquisition time efficiency dictates maximal filling of each TR period with spectrally interleaved

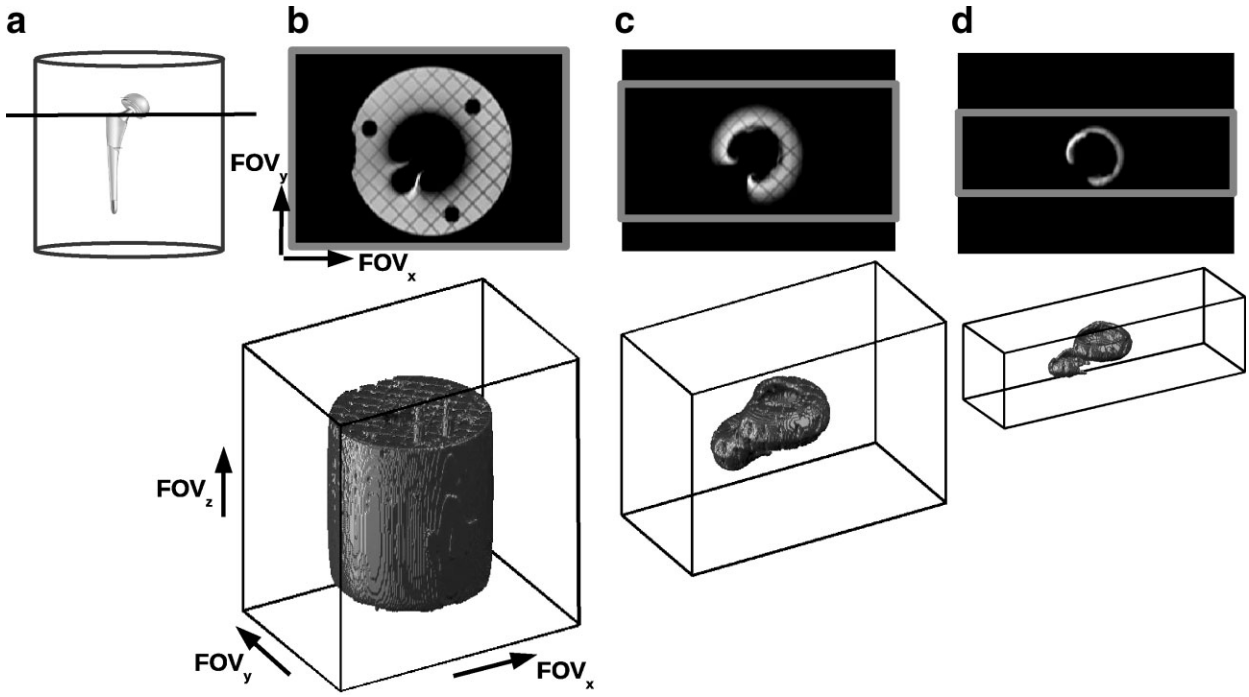

FIG. 3. (**a**) Setup for CoCr/Ti total hip joint prosthesis (Phantom A). The acrylic support structure and grid is not shown in the illustration. The displayed axial slice is indicated. (**b**) Axial slice of on-resonance ($\Delta\nu_0^{RT} = 0$) MAVRIC sub-image and volumetric rendering of acquired signal. The box in the MRI image and parallelpiped around the volumetric rendering represent the full fields of view in each dimension. (**c**) Axial slice of near off-resonance ($\Delta\nu_0^{RT} = 2$ kHz) MAVRIC subimage and volumetric rendering of acquired signal with fields of view adapted in k_y and k_z. (**d**) Similar representations of a far off-resonance ($\Delta\nu_0^{RT} = 6$ kHz) MAVRIC subimage. CoCr components in the utilized hip assembly are the acetabular ball and the joint connecting the ball to the Ti shaft, thus explaining the locality of off-resonance spins to these regions.

echo-trains. The number of interleaves that can be collected in a given TR period is determined by the utilized CPMG echo-train length (ETL).

Three-dimensional Cartesian slab-selection was not utilized in the presented MAVRIC acquisitions (i.e. no slab-selection gradients were applied). To prevent unacceptably long acquisition times, the use of local RF coils may therefore be required to limit the active field-of-view for some arthroplasty imaging applications (such as total hip replacements).

Adaptive Phase Encoding

Significant scan time improvements are enabled in the MAVRIC method through an adaptive phase-encoding principle. This principle rests on the observation that off-resonance acquisitions tend to impact spins in the near vicinity of implant interfaces. For these off-resonance images, the number of phase-encodes in k_y and k_z can be reduced without sacrificing image resolution.

Figure 3 illustrates the adaptive phase-encoding principle. The geometry of the setup for Phantom A (CoCr/Ti total hip replacement embedded in an acrylic grid) is illustrated in Fig. 3a.

In the presented adaptive phase-encoding example, an axial three-dimensional imaging strategy is applied, where k_x is the readout dimension and k_y/k_z are the phase-encoded dimensions (this convention will be maintained throughout the images presented in this work). Figure 3b provides an axial MR image and a volumetric rendering of the active MR signal for an on-resonance ($\Delta\nu_0^{RT} = 0$) acquisition. The position of the displayed slice is indicated on the phantom illustration in Fig. 3a. The box in the axial image and the parallelpiped around the volumetric rendering represent the full fields of view utilized in each dimension. An off-resonance image ($\Delta\nu_0^{RT} = 2$ kHz) is displayed in Fig. 3c. The active signal is clearly reduced and is more localized to the implant. The gray box and parallelepiped are reduced to demonstrate an adaptive phase-encoding reduction of 30% in k_y and 38% in k_z in the image acquisition of this spectral bin. A far-off resonance acquisition ($\Delta\nu_0^{RT}$ = 6 kHz) with further active signal reduction is displayed in Fig. 3d. Adaptive phase-encoding reductions of 43% and 67% are indicated for k_y and k_z, respectively.

To apply the adaptive phase-encoding principle to MAVRIC acquisitions, off-resonance images are collected at reduced phase-encoded fields of view (FOV) and accordingly reduced numbers of phase-encode steps needed to maintain consistent image resolution across the spectral acquisitions. Reducing the numbers of phase-encodes in k_y and k_z, greatly reduces the acquisition time for many off-resonance images. Images collected at adaptive phase-encoded settings are combined with full-FOV images by zero-filling adaptive-encoded image domains.

Application of adaptive phase-encoding principles requires that not all spectral interleaves are collected in a single TR period. Each phase-encoding setting must

operate on independent sets of spectral bins acquired in separate TR periods. The current implementation of the MAVRIC technique predetermines this distribution of spectral bins. For example, consider an image requiring acquisition of 21 spectral bins. One TR period could collect seven spectral bins (low $\Delta\nu_0^{RT}$ settings) under full phase-encoding, whereas the next two TR periods could each collect seven more spectral bins (higher $\Delta\nu_0^{RT}$ settings) under reduced phase-coded conditions. Using such a strategy where the interleaving structure is pre-arranged, ETL settings can be adjusted to maximally fill desired TR periods. In the present implementation, a chosen TR period of 800 msec is most efficiently acquired with an ETL of 8. Alternatively, a chosen TR period of 2.4 sec can more efficiently be acquired with an ETL of 20.

The data presented in this work utilizes a conservative adaptive phase-encoding application whereby the k_y and k_z encodings are reduced by roughly 30% and 35%, respectively, for all images collected beyond 4 kHz of frequency offset. More sophisticated adaptive phase-encoding approaches are feasible and will assist in further acquisition time reductions. Prior knowledge of implant compositions (e.g. titanium, cobalt-chromium) and geometries (e.g. total knee vs total hip) can also enhance the robustness and efficacy of adaptive phase-encoding approaches.

Composite Image Formation

MAVRIC subimages can be combined either through a maximum-intensity-projection (MIP), or a sum-of-squares (SOS) process. Though the SOS process results in superior composite image SNR, care must be taken in its application. Using either (a) RF pulses designed with the SLR pulse design algorithm (23) to produce boxcar frequency response profiles or (b) hard pulses with sinc frequency responses is prohibitive to SOS combination of MAVRIC subimages.

Construction of composite images without significant combination artifacts necessitates a limited amount of spectral overlap between spectrally adjacent subimages. Figure 4a illustrates the spectral spin response to an ideal boxcar spectrally selective refocusing RF pulse (bandwidth 2.25 kHz) and a RF refocusing pulse with Gaussian spectral profile (FWHM = 2.25 kHz). Figure 4b displays the spectral response of a greatly dispersed spin-ensemble spanning ±15 kHz to SOS combination of 29 RF pulses as indicated in Fig. 4a with center frequencies separated by $\Delta\nu_0^{RT} = 1$ kHz and assuming spectrally uniform and independent excitation processes. It is clear that the spectral response to slightly overlapping boxcar pulses has a periodic amplitude modulation. This transfers into a spatial intensity artifact in composite MAVRIC images. Although a MIP could instead be applied to the ideal boxcar pulses to achieve a flat composite spectral response, this results in lower composite-image SNR and can suffer from residual combination artifacts at spectral boundaries in the image domain.

It is clear in Fig. 4b that the indicated Gaussian refocusing pulses produce a primarily flat SOS spectral response. SOS combination of the Gaussian profiles also produces smoother composite-image transitions across spectral image-domain boundaries. For application in the presented MAVRIC technique, 135° refocusing pulses with Gaussian spectral profiles (FWHM = 2.25 kHz) were developed using a Kaiser-Bessel window within the SLR pulse-design algorithm. To maintain the assumption of spectrally independent excitation processes, 90° selective SLR excitation pulses with flat spectral responses spanning the Gaussian refocusing profiles were utilized.

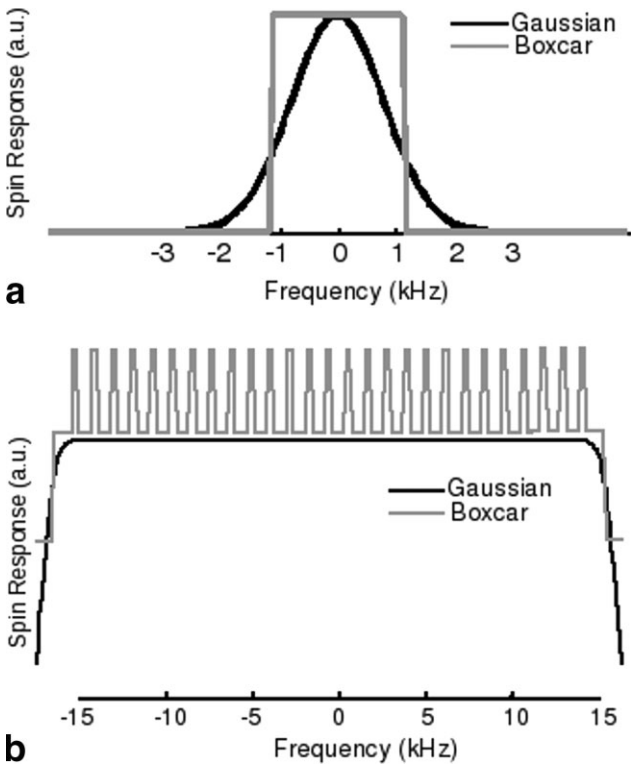

FIG. 4. (**a**) On-resonance spectral responses of spins to Gaussian (FWHM = 2.25 kHz) and 2.25 kHz boxcar spectrally selective RF refocusing pulses. (**b**) Sum of squares spectral responses to a series of 29 pulses spectrally separated by $\Delta\nu_0 = 1$ kHz.

Imaging and Reconstruction Parameters

The required spectral coverage of MAVRIC images is dependent on both the desired proximity of imaging signal near prostheses and the material compositions of each prosthesis. The images presented here were acquired with the intention of maximizing signal proximity to CoCr and Ti implants. Spectral information was therefore collected beyond empirically observed limits of resolvable signal. This resulted in longer scan times than are likely to be required for clinical utility, but guaranteed a full demonstration of the method's capability.

MAVRIC images were zero filled by factors of three in k_y and two in k_z. 2D-FSE images were acquired with 1.4 kHz (Phantom A and in vivo) and 1.0 kHz (Phantom B) selective SLR excitation and refocusing RF pulses over geometries identical to those of the MAVRIC images. Zero filling of k_y by a factor of three was performed on all 2D FSE images.

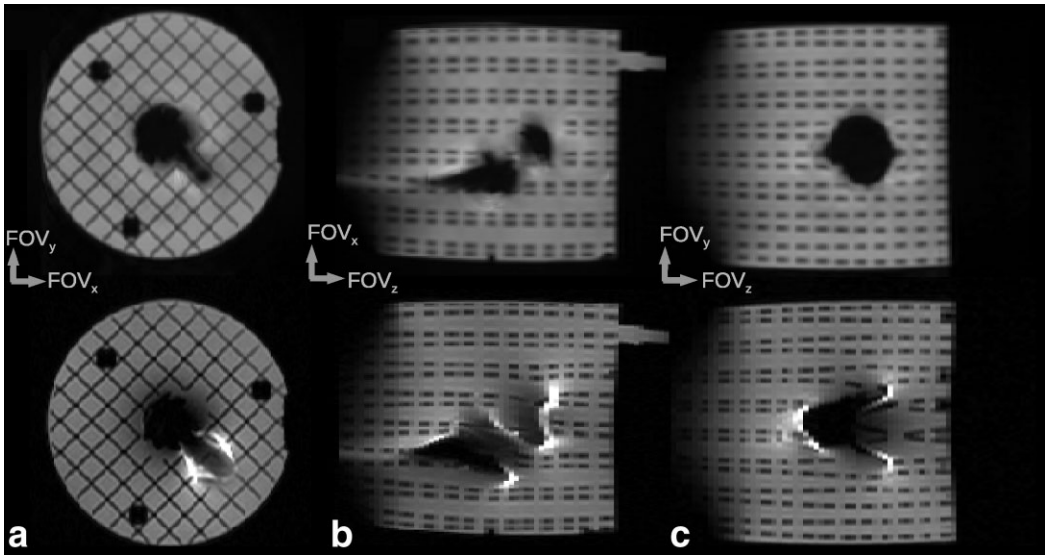

FIG. 5. (**a**) Axial MAVRIC (top row) and 2D-FSE (bottom row) images on Phantom A (CoCr/Ti total hip replacement), (**b**) sagittal reformatted Images, and (**c**) coronal reformatted images.

All presented images were collected at ±125 kHz readout bandwidths, which is significantly higher than previously published approaches to 2D-FSE imaging near metal implants (7,20).

RESULTS

Figure 5 presents imaging results on Phantom A. Axial MAVRIC images were collected with TE = 35 msec, TR = 600 msec, an echo-train-length (ETL) of 8, and 1 mm × 2 mm × 3 mm pixel resolutions over 27.0 cm × 16.2 cm × 24.0 cm fields-of-view in k_x, k_y, and k_z, respectively. Twenty-seven spectrally unique images were acquired spanning ±13 kHz of frequency offsets, requiring 23 min of acquisition time. Figure 5a displays an axial MAVRIC image (top row) near the cobalt-chromium acetabular component of the total hip replacement. The 2D FSE image (bottom row) shows significant distortion and artificial intensity modulation in the vicinity of the implant. Any residual image distortion in the MAVRIC image is limited to the highly localized regions where the local ΔB_0 field gradients are on the order of the readout imaging gradient (where small image displacements can "pile-up"). The structure of the implant boundary and its near surroundings is greatly improved in the MAVRIC image. To demonstrate the benefits in removing slice-selective distortions, sagittal (Fig. 5b) and coronal (Fig. 5c) reformats of both the MAVRIC and 2D-FSE images are also displayed. In addition to the clear image distortions in the 2D FSE images (bottom row), note the curvature of the acrylic gridlines in the vicinity of the implant. As seen in the MAVRIC images (top row), this curvature is artefactual. The gridlines should be straight in the sagittal and coronal planes.

Imaging results on Phantom B are presented in Fig. 6. Axial MAVRIC images on Phantom B were collected with TE = 20 msec, TR = 2,400 msec, ETL = 24, and 1 mm × 2 mm × 3 mm pixel resolutions over 28.0 cm × 16.8 cm × 18.0 cm fields-of-view in k_x, k_y, and k_z, respectively. Thirty-three spectrally unique images were acquired spanning ±17 kHz of frequency offsets, requiring 27 min of acquisition time. Figure 6a displays an axial MAVRIC image slicing through both the plastic and cobalt-chromium implant structures (Fig. 1a provides the setup for this phantom). When compared with the 2D-FSE image (Fig. 6b), the MAVRIC image shows far greater similarity to the implant structure indicated by the plastic component.

In vivo images near a total knee replacement are displayed in Fig. 7. MAVRIC images were acquired in vivo with TE = 20 msec, TR = 2400 msec, ETL = 22, and and 1 mm × 2 mm × 3 mm pixel resolutions over 27.0 cm × 16.2 cm × 24.0 cm fields-of-view in k_x, k_y, and k_z, respectively. Twenty-one spectrally unique images were acquired spanning ±11 kHz of frequency offsets, requiring 25 min of acquisition time. The left column in Fig. 7 displays MAVRIC images in the (A) axial plane, (B) reformatted coronal plane, and (C) reformatted sagittal plane. 2D-FSE images acquired over the same geometry are presented in the right column of Fig. 7. Implant interfaces that are clearly identified in the MAVRIC images are noticeably distorted in the 2D-FSE images (indicated by arrows). Such interfaces are where crucial early diagnostic indications of particle disease and osteolysis would be located. Figure 8a displays a volumetric rendering of a femur using a T_1-weighted MAVRIC acquisition (TR = 600 msec). Using the MAVRIC image, an automatic thresholding and region-growing scheme was utilized to render the displayed arthroplasty-sculpted femur. A three-dimensional rendering of a femoral implant component similar to that installed in the arthroplasty patient is displayed in Fig. 8b. The shape of the installed implant is clearly identified in the volumetric rendering of the bone, including the support posts and flattened surface with the implant. An automatic segmentation using the 2D-FSE image was not feasible. This is a predictable result given the geometric

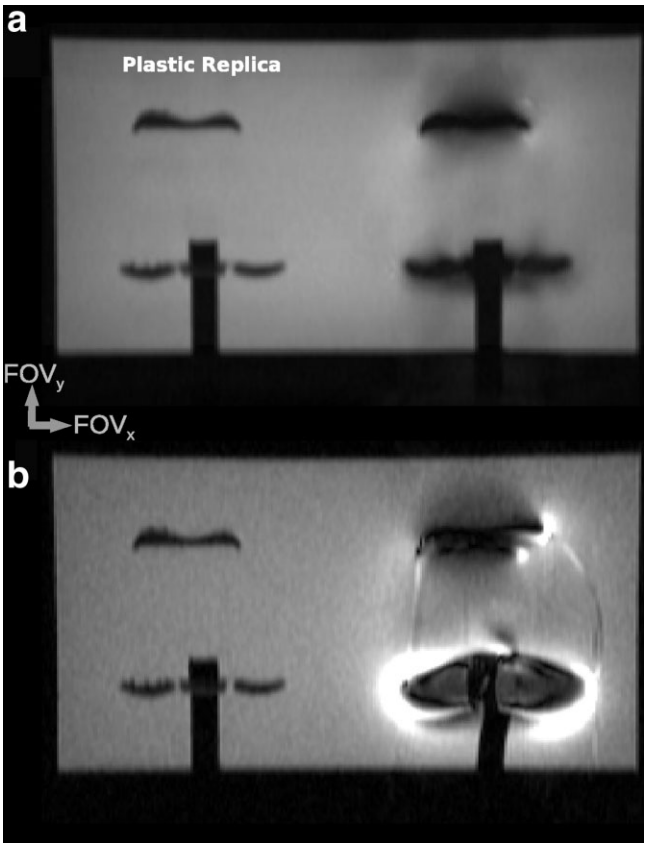

FIG. 6. Axial MAVRIC image (**a**) and 2D-FSE Image (**b**) on Phantom B (CoCr/Ti femoral component from a total knee replacement and plastic cast replica).

and intensity variations clearly identified in the 2D-FSE images presented in Fig. 7.

DISCUSSION

Both phantom and in vivo imaging results show greatly reduced B_0 artifacts near metal implants through application of the MAVRIC technique. With the MAVRIC technique, significantly increased diagnostic capabilities are attained with existing clinical MR imaging hardware. In the immediate vicinity of most metal implants, conventional MR image-based information can be significantly compromised by the tremendous image distortions caused by far off-resonance (4–5 kHz) spins. Further away from implant interfaces, while conventional images may not show obvious signs of distortion, significant image misrepresentations are still possible (exemplified by the gridline curvature seen in the 2D-FSE images of Fig. 5). The methods introduced in this work can significantly improve the quality of MR images near metal implants by removing all distortion in the slice-select dimension and greatly reducing its effects in the readout dimension.

Although the application of spectral image interleaving and adaptive phase-encoding enables acquisition of MAVRIC images in reasonable scan-times (20–25 min for 20–30 kHz of spectral coverage), further acquisition acceleration is needed to enable widespread clinical viability. Such acceleration will be required to minimize scan times and improve image resolution. Parallel imaging is a viable means to such acceleration. Initial acceleration simulations using multichannel MAVRIC acquisitions with the ARC (24) autocalibrated parallel imaging technique have shown little or no adverse effects near metal implants. This is due to the hybrid-space autocalibrated reconstruction process utilized in the ARC technique (25). Effective acquisition accelerations of up to 3× have been successfully simulated. Future work will integrate these parallel acquisition techniques with the MAVRIC method.

Another potential means to image acceleration is through the compressed-sensing algorithm (26,27). When applied to MR imaging, compressed sensing reduces acquisition time through randomized k-space undersampling and iterative reconstruction using a least-squares conjugate-gradient optimization in the undersampled dimensions

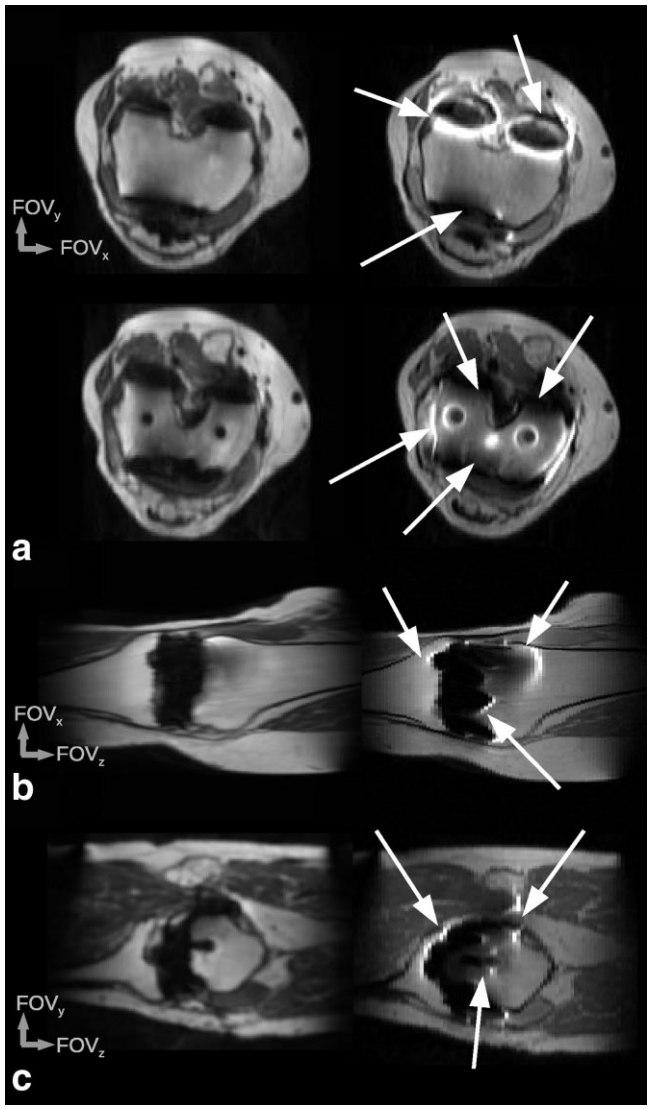

FIG. 7. (**a**) Axial MAVRIC (left column) and 2D-FSE (right column) images on a human subject with CoCr/Ti total knee replacement, (**b**) coronal reformatted images, and (**c**) sagittal reformatted Images. Arrows indicate regions of intense geometric distortion In the 2D-FSE images that are greatly improved in the MAVRIC images.

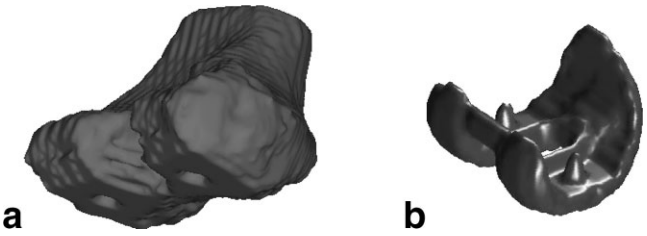

FIG. 8. (**a**) Volumetric rendering of a femur from a T_1-weighted MAVRIC acquisition. (**b**) Three-dimensional rendering of a femoral implant component similar to that installed on the displayed femur.

(28). The efficiency and accuracy of compressed sensing relies upon transformation of the image domain to sparse transform domains. This is commonly accomplished through wavelet transforms and/or gradient transforms. Off-resonance images in MAVRIC acquisitions are sparse in both the image and gradient domains. Much like angiography applications, this provides a convenient platform for compressed sensing acquisition acceleration strategies (29).

The only visibly identifiable B_0 artifacts in MAVRIC images arise from intense local gradients causing signal from multiple pixels to converge to a single pixel (the "pile-up" effect). Since the maximum distortion in a MAVRIC image is on the order of a single pixel width, these artifacts are highly localized. The chosen orientation of the readout direction can have a slight effect on these residual artifacts. Although swapping of phase and frequency in the axial plane does not significantly alter the quality of MAVRIC images, images in the coronal or sagittal planes will benefit from placing the in-plane phase-encode dimension along the $\hat{z}$ axis. This is due to the generally increased severity of induced B_0 gradients in the direction of the applied magnetic field. Despite the limited and nuanced nature of residual "pile-up" effects, it would be preferable to rid the composite images of all B_0 artifacts. A potential means to reduce these residual artifacts could utilize the MAVRIC method's inherent spectral resolution. Field maps can be constructed from MAVRIC images by assigning each spatial location the frequency offset value ($\Delta\nu_0^{\mathrm{RT}}$) utilized in acquiring the subimage with maximum intensity at that location. The field map in Fig. 1b is constructed using this technique. Future investigations will seek to apply a limited post-acquisition repair in the readout dimension of MAVRIC images using this inherent field-map information.

Comparison of the plastic replica and metal implant in the MAVRIC image of Fig. 6a shows that a small amount of signal near the implant is not captured in the MAVRIC image. Further analysis of MAVRIC data from this phantom shows that the missing signal cannot be gained from further spectral coverage. It is hypothesized that B_1 effects are related to this signal reduction. Close inspection also reveals slight intensity modulations of slow spatial variation near the implant in Fig. 6a. Because B_0 intensity artifacts in MAVRIC images are of high spatial variation (on the order of a pixel), these effects are also suspected to be of B_1 origin. In the absence of B_1 effects, a MAVRIC image of sufficient spectral coverage could theoretically provide reliable signal up to roughly 1 pixel in the readout dimension from implant interfaces (or 1mm using the imaging specifications applied in the presented work). This conceptual boundary is estimated from the analysis presented in Section "Three-dimensional Imaging Near Metal Implants". However, in practice the effects of B_1-induced signal reduction can alter this theoretical capability. Although B_1 perturbations near metallic interventional devices and implants have been studied and analyzed in vitro (12,13), the impact of such perturbations on CPMG echo trains and composite MAVRIC images will be the subject of further analysis and modeling.

The precise resolution of composite MAVRIC images varies spatially with implant-induced B_0 distributions and is dependent on chosen readout bandwidths, RF bandwidths, and spectral bin separations. Spins imaged by adjoining spectral bins have a slightly larger point-spread (in the readout direction) in composite MAVRIC images than that inherent to individual (3D-FSE) images. This point-spread enhancement is subtle and is not symmetric in the readout direction due to the use of Gaussian RF pulses, which results in nonreciprocal intensities for spins independently imaged by adjoining spectral bins. In other words, a spin resonating in the tail of a Gaussian profile may be pushed further into the image from an adjoining spectral bin, but it will possess dramatically reduced signal intensity and contribute little to the point-spread. The visibility of this effect is highly dependent on the local B_0 field gradient in the readout direction, which determines the spatial proximity of adjoining spectral bins. A further resolution consideration involves the T_2* truncation of spin-echo envelopes. Although the MAVRIC technique utilizes high bandwidth readout sampling (which will reduce such truncation effects), regions of severe B_0 gradients can cause additional localized blurring. An example of the varying point-spread in MAVRIC images can be found in Fig. 6a, where a small amount of localized blurring can be identified near the CoCr implant. Quantitative analysis and numerical simulations of the MAVRIC point-spread are beyond the scope of this work. However, such investigations are the subject of ongoing investigation.

The inherent SNR of composite MAVRIC images is given by quadrature addition of SNR from the individual subimages. Because the subimages do not have equal signal contributions, the resulting SNR is less than the $\sqrt{N_I}$ improvement (where N_I are the number of component images) expected from a conventional sum-of-squares image combination (where each image would have equal signal intensity). Though potential SNR improvements may be possible with alternative composite image formations schemes, SNR is not a significant limitation in the current MAVRIC implementation.

For all implant scenarios presented in this work, less than 1% of the available signal was found beyond 10 kHz off-resonance. Therefore, it is likely that clinical applications of the MAVRIC technique would benefit from trading off the small amount of information in the furthest off-resonance images for reductions in total acquisition time. It should be noted that less commonly encountered implants (such as MR-compatible stainless steel hips or knees) may still benefit from the extended spectral coverage applied in the data presented here. Future clinical investigations will

further illuminate the various successes and tradeoffs of the MAVRIC technique for a variety of implant geometries and compositions.

Images collected using the presented MAVRIC technique exhibit tissue contrast that differs slightly from conventional 2D-FSE and 3D-FSE images. The broad spectral coverage inherent to the MAVRIC technique may introduce magnetization transfer (30) effects and/or develop alternative contrast between chemical species (e.g. water and fat). Comprehension of these potential contrast mechanisms and their impact on clinical applications will also require further investigation.

In conclusion, the applied techniques and initial results of a novel technique for imaging in the vicinity of metal implants have been presented. Preliminary results show that large gains in image quality can be attained using this method in place of existing clinical approaches to imaging of arthroplasty patients. Further development of promising acquisition acceleration mechanisms will greatly enhance the clinical viability of the technique and may offer improved diagnostic assessment and planning for arthroplasty revision procedures.

ACKNOWLEDGMENTS

The authors would like to thank Dr. Hollis Potter, MD for assistance in establishing the clinical context of the presented methods. Dr. Patrick LeRoux, Dr. Anja Brau, Dr. Weitian Chen, Dr. Reed Busse, Dr. Hari Hariharan, Dr. Manoj Saranathan, Dr. Patrick Virtue, Troy Lewein, and Dr. Graeme McKinnon also provided valuable technical discussions and/or assistance to this work.

REFERENCES

1. Kurtz S, Mowat F, Ong K, Chan N, Lau E, Halpern M. Prevalence of primary and revision total hip and knee arthroplasty in the United States from 1990 through 2002. J Bone Joint Surg Am 2005;87:1487–1497.
2. Kurtz S, Mowat F, Ong K, Chan N, Lau E, Halpern M. Projections of primary and revision hip and knee arthroplasty in the United States from 2005 to 2030. J Bone Joint Surg Am 2007;89:780–785.
3. Sochart DH. Relationship of acetabular wear to osteolysis and loosening in total hip arthroplasty. Clin Orthop 1999;363:135–150.
4. Schmalzried TP. Wear in total hip and knee replacements. J Bone Joint Surg Am 1999;81:115–136.
5. Gallo J, Kaminek P, Ticha V, Rihakova P, Ditmar R. Particle disease, a comprehensive theory of peroprosthetic osteolysis: A review. Biomed Pap 2002;146:21–28.
6. Lavernia CJ. Cost-effectiveness of early surgical intervention in silent osteolysis. J Arthroplasty 1998;13:277–279.
7. Potter HG, Nestor BJ, Sofka CM, Ho ST, Peters LE, Salvati EA. Magnetic resonance imaging after total hip arthroplasty: evaluation of perioprosthetic soft tissue. J Bone Joint Surg Am 2004;86:1947–1954.
8. Puri L, Wixson RL, Stern SH, Kohli J, Hendrix RW, Stulberg SD. Use of helical computed tomography for the assessment of acetabular osteolysis after total hip arthroplasty. J Bone Joint Surg Am 2002;84:609–614.
9. White LM, Kim JK, Mehta M, Merchant N, Schweitzer ME, Morrison WB, Hutchison CR, Gross AE. Complications of total hip arthroplasty: MR imaging–initial experience. Radiology 2000;215:254–262.
10. Shellock FG. Magnetic resonance safety update 2002: Implants and devices. J Magn Reson Imag 2002;16:485–496.
11. Park YS, Hwang SK, Choy WS, Kim YS, Moon YW, Lim SJ. Ceramic failure after total hip arthroplasty with an alumina-on-alumina bearing. J Bone Joint Surg Am 2006;88:780–787.
12. Graf H, Lauer UA, Berger A, Schick F. RF artifacts caused by metallic implants or instruments which get more prominent at 3 T: An in vitro study. Magn Reson Imag 2005;23:493–499.
13. Graf H, Steidle G, Martirosian P, Lauer UA, Schick F. Effects on MRI due to altered RF polarization near conductive implants or instruments. Med Phys 2006;33:124–127.
14. Ramos-Cabrer P, van Duynhoven JPM, van der Toor A, Nicolay K. MRI of hip prostheses using single-point methods: In vitro studies towards the artifact free imaging of individuals with metal implants. Magn Reson Imag 2004;22:1097–1103.
15. Venook RD, Matter NI, Ramachandran M, Ungersma SE, Gold GE, Giori NJ, Macovski A, Scott GC, Conolly SM. Prepolarized magnetic resonance imaging around metal orthopedic implants. Magn Reson Med 2006;56:177–186.
16. Butts K, Pauly JM, Daniel BL, Kee S, Norbash AM. Management of biopsy needle artifacts: Techniques for RF-refocused MRI. J Magn Reson Imag 1999;9:586–595.
17. Butts K, Pauly JM, Gold GE. Reduction of blurring in view angle tilting MRI. Magn Reson Med 2005;53:418–424.
18. Lu W, Pauly KB, Gold GE, Pauly JM, Hargreaves BA. Towards Artifact-free MRI near metallic implants. In Proceedings of 16th Annual Meeting of the ISMRM, Toronto, ON, Canada, 2008. p 838.
19. Koch KM, Rothman DL, de Graaf RA. Optimization of static magnetic field homogeneity in the human and animal Brain In Vivo. Progr NMR Spectrosc Forthcoming, doi:10.1016/j.pnmrs.2008.04.001.
20. Kolind SH, MacKay AL, Munk PL, Ziang Q. Quantitative evaluation of metal artifact reduction techniques. J Magn Reson Imag 2004;20:487–495.
21. Koch KM, Hinks RS. Empirical and computed B_0 perturbations induced by metallic implants. In Proceedings of 16th Annual Meeting of the ISMRM, Toronto, ON, Canada, 2008. p 1180.
22. Schenck JF. The role of magnetic susceptibility in magnetic resonance imaging: MRI magnetic compatibility of the first and second kinds. Med Phys 1996;23:815–850.
23. Pauly JM, Le-Roux P, Nishimura D, Macovski A. Parameter relations for the Shinnar-Le Roux selective excitation pulse design algorithm. IEEE Trans Med Imag 1991;10:53–65.
24. Beatty PJ, Hargreaves BA, Gurney PT, Nishimura DG. A method for non-Cartesian parallel imaging reconstruction with improved calibration. In Proceedings of 14th Annual Meeting of the ISMRM, Seattle, WA, USA, 2006. p 2462.
25. Brau AC, Beatty PJ, Skare S, Bammer R. Comparison of reconstruction accuracy and efficiency among autocalibrating data-driven parallel imaging methods. Magn Reson Med 2008;59:382–395.
26. Candes E, Romberg J, Tao T. Robust uncertainty principles: Exact signal reconstruction from highly incomplete frequency information. IEEE Trans Inf Theory 2006;52:489–509.
27. Donoho D. Compressed sensing. IEEE Trans Inf Theory 2006;52:1289–1306.
28. Lustig M, Donoho D, Pauly JM. Sparse MRI: The application of compressed sensing for rapid MR imaging. Magn Reson Med 2007;58:1182–1195.
29. King KF. Combining compressed sensing and parallel imaging. In Proceedings of 16th Annual Meeting of the ISMRM, Toronto, ON, Canada, 2008. p 1488.
30. Wolf SD, Balaban RS. Magnetization contrast (MTC) and tissue water proton relaxation in vivo. Magn Reson Med 1989;10:135–144.